Check for updates

Highly dispersed ultrafine PtCo alloy nanoparticles on unique composite carbon supports for proton exchange membrane fuel cells†

Lingling Zhang,[a] Tong Liu,[a] Xiaokang Liu,[a] Sicheng Li, [iD][a] Xue Zhang,[a] Qiquan Luo, [iD][c] Tao Ding, [iD] *[a,b] Tao Yao [iD][a,b] and Wei Zhang*[a,b]

The design of highly efficient and robust platinum-based electro-catalysts is pivotal for proton exchange membrane fuel cells (PEMFC). One of the long-standing issues for PEMFC is the rapid deactivation of the catalyst under working conditions. Here, we report a simple synthesis strategy for ultrafine PtCo alloy nano-particles loaded on a unique carbon support derived from a zeolitic imidazolate framework-67 (ZIF-67) and Ketjen Black (KB) composite, exhibiting a remarkable catalytic performance toward the oxygen reduction reaction (ORR) and PEMFC. Benefitting from the N-doping and wide pore size distribution of the composite carbon supports, the growth of PtCo nanoparticles can be evenly restricted, leading to a uniform distribution. The Pt-integrated catalyst delivers an outstanding electrochemical performance with a mass activity that is 8.6 times higher than that of the commercial Pt/C catalyst. Impressively, the accelerated durability test (ADT) demonstrates that the hybrid carbon support can significantly enhance the durability. Theoretical simulations highlight the synergistic contribution between the supports and the PtCo nano-particles. Moreover, hydrogen–oxygen fuel cells assembled with the catalyst exhibited a high power density of 1.83 W cm^{-2} at 4 A cm^{-2}. These results provide a new opportunity to design advanced catalysts for PEMFC.

Introduction

High-efficiency electrocatalysts applied to the oxygen reduction reaction (ORR) play a pivotal role in the development of fuel cells, which is a promising energy technology for the sustainable development of human society.[1,2] Over the years, precious metal group nanocrystals (PMG NCs) have been strategically loaded on support materials to make full use of the precious metal and diminish the cost of proton exchange membrane fuel cells (PEMFC).[3–6] Until now, carbon supports have been widely used for PMG NCs.[7–9] The physical properties of the carbon support layer can have a big impact on the performance of the fuel cells.[10] Thus, it is of great concern to optimize the activity and durability of carbon-supported PMG NCs for the ORR occurring at the fuel cell cathode.[11,12]

A low-Pt loading membrane electrode assembly (MEA) with high performance is critical to the economic viability of PEMFC for the transportation industry.[13] Extensive research has been aimed to minimize Pt usage in fuel cells, leading to the development of transition metal alloy catalysts, notably platinum–cobalt (PtCo) catalysts, known for their enhanced ORR kinetics.[14] However, the durability of PtCo catalysts can be impacted by not only the intrinsic properties of the catalyst particles, but also their interactions with the carbon support. Refined particles can enable better electrocatalytic activity resulting from the enhanced specific surface areas,[11] and suitable carbon supports are crucial for maintaining metal particle dispersion and providing proton transport pathways.[15,16] Additionally, carbon supports are extremely vulnerable to corrosion and oxidation under high operating potential and low pH conditions.[17] As a result, developing an efficient and robust support is urgent for resolving these problems. In view of the MEA and the construction of catalyst layers, the employment of carbon supports is absolutely necessary. One of the important physical differences between variants of carbon supports is the porosity of the carbon particles and aggregates.[10] The porosity and composition affect how the Pt particles and ionomer are dispersed in and around the carbon particles, leading to the different performances. Recently, Ketjen Black (KB) has attracted widespread attention with an ultrahigh surface area. However, a separate carbon support may be more prone to corrosion, especially under high potential and transi-

aNational Synchrotron Radiation Laboratory, School of Nuclear Science and Technology, University of Science and Technology of China, Hefei, 230029, P. R. China. E-mail: dingtao@ustc.edu.cn, zhangw94@ustc.edu.cn
bKey Laboratory of Precision and Intelligent Chemistry, Hefei National Research Center for Physical Sciences at the Microscale, University of Science and Technology of China, Hefei 230026, P. R. China
cInstitutes of Physical Science and Information Technology, Anhui University, Hefei, 230601, P. R. China

ent conditions such as start-up/shut-down, as well as uneven dispersion of active Pt particles and limited pore size distribution. Meanwhile, zeolitic imidazolate frameworks (ZIFs), a sub-class of metal–Organic frameworks (MOFs) rich in micropores and N atoms, have long been utilized as the precursor for cathode catalysts.[18] Further investigation on constructing composite carbon supports is ongoing to meet the requirements of sufficient electron transfer, mass transport, and product release. In addition, a uniform particle size and unique N-modification can regulate the distribution of ionomers, as well as high dispersibility, and are considered as the key to enhance the durability of acidic catalysis.[19] Therefore, integrating Pt-based alloys into the composite support appears promising for balancing the activity and stability in PEMFC.[20,21] Moreover, composite carbon supports provide additional active sites and strong interactions, thus synergistically enhancing the efficient activity of ORR catalysis.

Here, we report a composite carbon to support ultrafine platinum–cobalt alloy nanoparticles for efficient ORR electrocatalysis in PEMFC. Uniform ultrafine nanoparticles were precisely synthesized, contributing to the hybrid support's expansive pore size distribution (PSD). This was achieved by integrating KB and ZIF-derived NCs as a support, followed by the impregnation and high-temperature reduction techniques. The resulting PtCoNC catalyst exhibited a high mass activity of 0.86 A mg_{Pt}^{-1} at 0.9 V *versus* the reversible hydrogen electrode (*vs.* RHE), which is 8.6 times higher than that of commercial Pt/C. Impressively, it maintained 92% of its activity after 15 000 potential cycles. Additionally, this hybrid catalyst delivers a voltage of 0.45 V at the current density of 4.0 A cm^{-2} in a hydrogen–oxygen fuel cell and reaches a power density of 1.83 W cm^{-2}. The advancement in Pt-based electrocatalysts not only amplifies the durability, but also dramatically enhances the activity, potentially paving the way for comprehensive research on integrated electrocatalysts within fuel cells and beyond.

Results and discussion

The key synthesis flowchart of the catalyst is depicted in Fig. 1a. Firstly, the precursors of ZIF-67NC and KB were subjected to ultrasonication with Pt(acac)$_2$ and Co(acac)$_2$, and then the precursors were heated at 700 °C for 15 h to obtain the composite catalyst (named PtCoNC). The scanning electron microscopy (SEM) image (Fig. 1b) shows the continuous porous network of composite carbon. The transmission electron microscopy (TEM) and high-resolution TEM images illustrate that PtCo nanoparticles are distributed homogeneously in the porous carbon with a uniform size of 2.1 nm with <5% deviation (Fig. 1c and Fig. S1†). Furthermore, powder X-ray diffraction (XRD) was carried out to identify the crystalline phase structures of catalysts. As demonstrated in Fig. 1e, the characteristic diffraction peaks of the samples in the XRD pattern matched well with those of CoPt$_3$ (standard PDF: 00-029-0049), translating to the Pt : Co atomic ratio of 3 : 1 con-

firmed by inductively coupled plasma-atomic emission spectrometry (ICP-AES). Observable lattice fringes indicate the *d*-spacing values of 0.222 and 0.193 nm of Pt$_3$Co, corresponding to the (111) and (200) crystalline planes, respectively. Notably, these diffraction peaks are located simultaneously between Pt (standard PDF: 01-087-0646) and Co (standard PDF: 01-089-4308), indicating that the catalyst is a PtCo alloy with an fcc phase structure. Moreover, compared to commercial Pt/C, an obvious diffraction peak shift was observed at 40.4°, which verifies the generation of shrinkage strain in the PtCo alloy, known for decreasing the Pt usage and enhancing the ORR intrinsic activity.[22] Meanwhile, the graphitization degree of the carbon support can also impact the lifetime of the fuel cell. Thus, the composite supports facilitate the loading and stabilization of Pt nanoparticles, forming smaller and more uniform PtCo nanoparticles than PtCoKB (Fig. S4†). During the fuel cell operation, carbon oxidation might degrade both the quality of the support and the retention and efficacy of catalyst particle.[17] However, these performance issues may be related to the fact that graphitized carbon tends to have fewer defect sites that bind to the catalyst material, resulting in poor dispersion and diminished performance.[23] Furthermore, graphitized carbon supports have lower Brunauer–Emmett–Teller (BET) surface areas. As shown in Fig. 1f, the Raman spectra exhibited the D band (1345 cm^{-1}) and G band (1597 cm^{-1}) and further confirmed the formation of C–N groups. Compared with PtCoKB, PtCoNC has a larger value of I_D/I_G (1.26), manifesting the enhanced defects after the combination, potentially attributable to N doping. The atomic ratio of N doping is 2.29% of the catalyst. Apart from hindering nanoparticles' agglomeration, the N doping carbon support can also affect metal bonding and prevent the shedding of alloys, avoiding Ostwald ripening. Additionally, compared with PtCoZIF67 (Fig. 1g and Fig. S5†), PtCoNC exhibits a higher BET specific surface area of 1346.8 m^2 g^{-1}, enhancing the exhaustive contact with reactive entities and active site exposure. As shown in Fig. 1g, the aperture distribution was analyzed using the Barrett–Joyner–Halenda (BJH) model.[8,20] The isotherm of PtCoNC exhibit a combination of type I (micropore), type IV (mesopore), and type II (macropores). The hysteresis loop appears to follow the H3-type behavior, thus revealing the distinct 3D amorphous porous structure and wide pore size distribution of the composite support. Due to the appropriate pore volume and high BET surface (Table S1†), rich active sites are exposed, and the mass transfer of reactants is greatly improved. This enhanced specific surface area is useful for dispersing metal NPs and exposing active sites, which agrees with the TEM results. The pore size distribution of PtCoNC is dominated by mesopores with a size of 4–7 nm, which improves the dispersion of active nanoparticles and endows the catalyst with both excellent ORR activities and transport properties.[24] Therefore, the balanced composite carbon support pore exhibits better pore size distribution and denser catalytic active sites, effectively promoting the electronic transfer, mass transport and product release, and enhanced corrosion resistance.
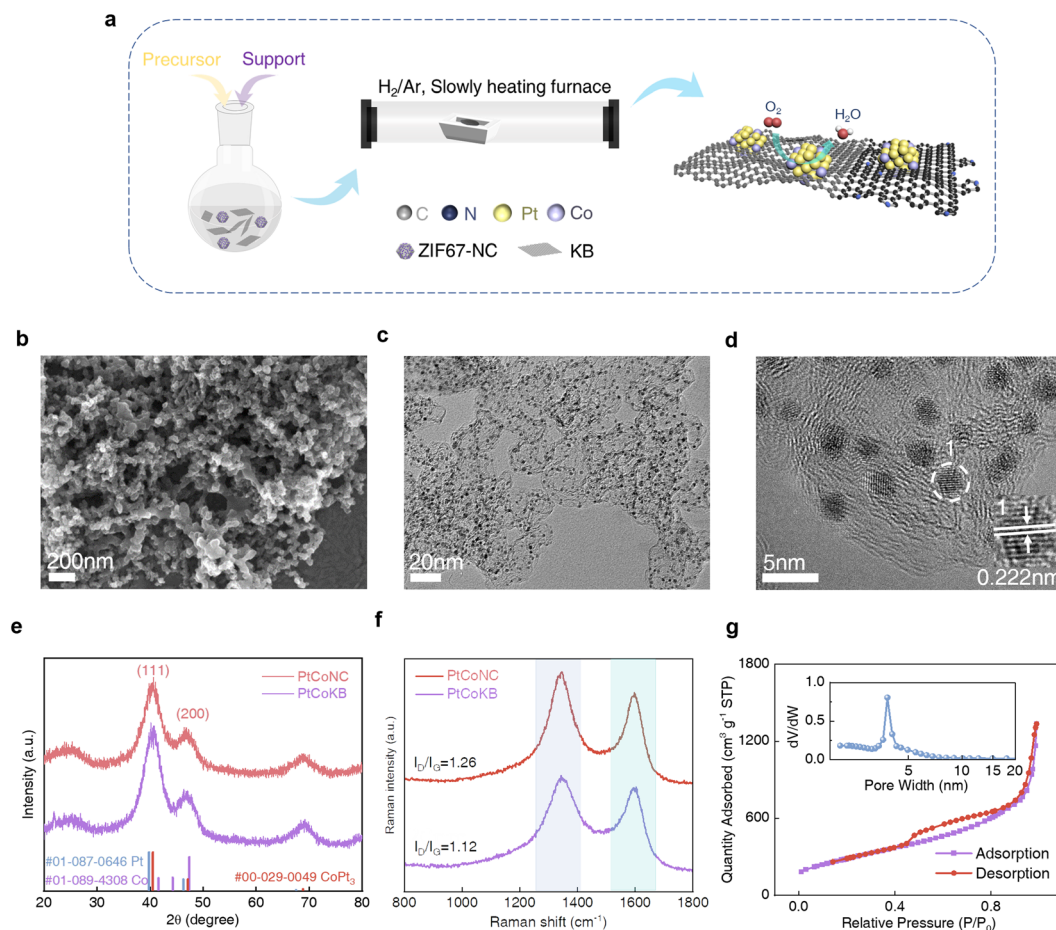
Fig. 1 (a) The key synthetic flowchart of the catalyst. (b) SEM image and (c and d) TEM image of PtCoNC. (e) XRD patterns. (f) Raman spectra of PtCoKB and PtCoNC. (g) N_2 adsorption/desorption isotherms of PtCoNC (inset shows the pore distribution of PtCoNC).

The electrochemical activities were then evaluated using the linear sweep voltammetry (LSV) technique in 0.1 M $HClO_4$ on a rotating ring-disk electrode at a rotating rate of 1600 rpm (Fig. 2a). PtCoNC shows a much higher half-wave potential ($E_{1/2}$) of 0.933 V *vs.* RHE, compared with PtCoKB (0.90 V *vs.* RHE), suggesting an improved intrinsic activity after forming the composite catalyst. The PtCoNC catalyst also exhibits a significantly high mass activity of 0.86 A mg_{Pt}^{-1} at the potential of 0.9 V *vs.* RHE (Fig. 2b), compared with PtCoZIF-67NC (0.61 A mg_{Pt}^{-1}), PtCoKB (0.31 A mg_{Pt}^{-1}), PtCoXC-72R (0.29 A mg_{Pt}^{-1}) and PtCoVC-72R (0.09 A mg_{Pt}^{-1}), which is even an 8.6-fold enhancement compared with commercial Pt/C (0.10 A mg_{Pt}^{-1}). The formation of water from molecular O_2 depends on the feasibility of O–O bond cleavage, which can be facilitated by the strong adsorption on the active site and charge polarization on the catalyst surface. It will easily polarize the electron cloud of the stable and neutral molecule. If less O–O cleavage occurs, the ORR proceeds *via* the two-electron pathway forming hydrogen peroxide.

To visually observe the difference in the hydrophilicity or hydrophobicity on the electrode surface, contact angle measurements were conducted. Fig. S6† shows that PtCoKB exhibited a contact angle (CA) of 100.35°, indicating a more hydrophobic surface. In contrast, PtCoNC possessed a wettable surface with a CA of 26.67°. Thanks to the advantageous composition of nitrogen doping, the hydrophilicity has been significantly improved, which proved to facilitate the accessibility of active sites to the electrolyte. The electrochemically active surface area (ECSA) of PtCoNC was calculated to be 93.1 m^2 g^{-1} with a higher roughness factor (RF), which is higher than PtCoKB (83.7 m^2 g^{-1}) (ESI Fig. S7 and Note 1†). Moreover, the RRDE experiment produced an extremely low ring current corresponding to H_2O_2 oxidation with only 1.42% of H_2O_2 being formed, which triggered us to deliver mechanistic insights into the catalytic phenomena (Fig. S10†). The different catalytic activities of these samples are mainly attributed to the differences in the carbon BET specific surface area, pore size distribution and carbon composition verified above. Moreover, an accelerated durability test (ADT) was conducted to evaluate the electrochemical stability of the catalysts. After 15k cycles, the half-wave potential only decreased by 8 mV and MA was retained by >91%, which is better than those of the commercial JM Pt/C catalyst (Fig. 2c). Except for $E_{1/2}$ and MA, the decrease of ECSA after 15k cycles can be ignored, implying that active sites tend to be a stable state (Fig. 2d). Moreover, to further verify the ORR performance of the catalysts, PEMFC
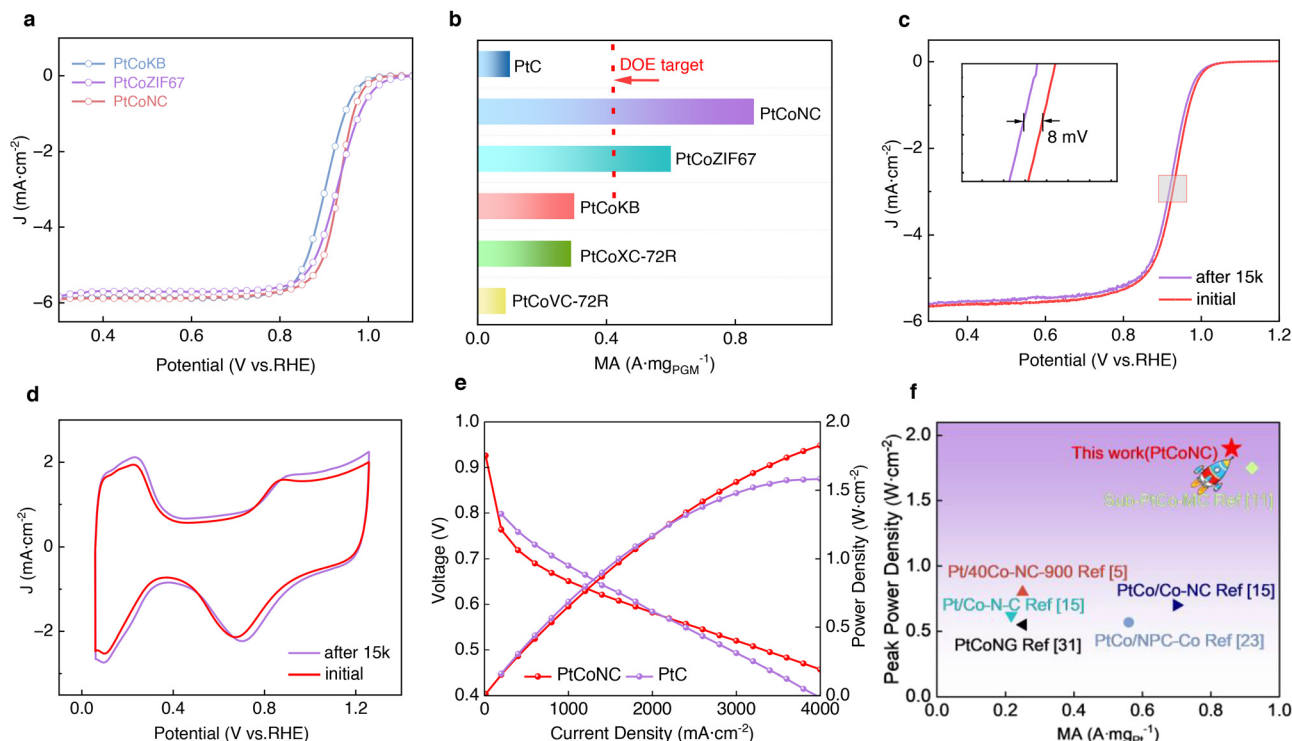
Fig. 2 Electrochemical tests. (a) LSV curves for PtCoKB, PtCoZIF67 and PtCoNC. (b) MA for PtC, PtCoNC, PtCoZIF67, PtCoKB, PtCoXC-72R and PtCoVC-72R. (c) RDE potential cycling stability tests for best performed PtCoNC, scanning rate 10 mV s⁻¹. (d) ECSA and (e) fuel cell performance with a comparison with the commercial Pt/C. Anode loading is 0.05 mg$_{Pt}$ cm⁻², cathode loading is 0.15 mg$_{Pt}$ cm⁻². (f) Performance comparison for PtCo with those of previous reports.

measurements were carried out. As shown in Fig. 2e, at a fuel cell current density of 2 A cm⁻² in the polarization curves, our PtCoNC catalyst exhibits a voltage of 0.58 V. It can also be observed that the highest power density can reach 1.83 W cm⁻² and exhibits a good discharge trend. At a high current density where more oxygen and protons are required for the reaction, the composite support allows the reactant oxygen gas to access the Pt active site, and consequently, substantially reduces the local oxygen-related mass transport resistance. In contrast to pure carbon as a support, the stability and activity improvement of Pt catalysts by constructing the composite support is remarkable. The PEMFC activity of PtCoNC is also at the superior level among the recently reported platinum-based electrocatalysts (Fig. 2f). These results clearly indicate that the synergy of the composite support can well boost the ORR activity and stability.[31,32]

X-ray photoelectron spectroscopy (XPS) was then employed to examine the surface chemistry of the catalyst. The full XPS survey spectrum mainly displays signals for Pt 4f, Co 2p, C 1s, N 1s and O 1s, consistent with the elemental composition of PtCoNC (Fig. S11†). As presented in Fig. 3a, the characteristic peak of N 1s is fitted into three distinct peaks: pyridinic-N (398.4 eV), pyrrolic-N (400.4 eV) and graphitic-N (402.2 eV). The graphitic-N atom is known to modulate the electron density of adjacent C atoms,[25] favouring electron transfer between C and N atoms. This process not only facilitates the dissociation of O₂ molecules from the carbon surface, but also

promotes the bonding between O and H atoms. Nevertheless, N doping on carbon is used to achieve a more uniform ionomer distribution on the entire catalyst surface.[19] Successful N doping in carbon materials offers robust anchoring points for PtCo alloys, which significantly accelerates the ORR kinetics of cathode catalysts, as evident from their electrochemical behaviour. Based on the peak fittings of Pt(0) 4f$_{7/2}$ (71.8 eV), Pt(II) 4f$_{7/2}$ (73.5 eV), Pt(0) 4f$_{5/2}$ (75.2 eV) and Pt(II) 4f$_{5/2}$ (76.9 eV), it is further demonstrated that Pt is mainly in the metallic state and has a small amount of coordination with carbon, nitrogen and oxygen atoms. Notably, the Pt(0) 4f$_{7/2}$ binding energy of PtCoNC manifests a discernible negative shift (0.2 eV) when compared with Pt/C (72.0 eV) (Fig. S12†). This shift underscores the modulation of the Pt electronic structure due to a combination of effects: the alloying influence from PtCo compounds and the strengthened interaction between the NC support and PtCo nanoparticles, thereby enhancing the ORR activity. In addition, Co signals in XPS is difficult to be observed, suggesting that Co is located inside the alloy after acid leaching. Thus, to obtain deep insight into the changes in the local electronic structure of PtCoNC, synchrotron radiation soft X-ray absorption spectroscopy (XAS) was employed. It is well known that X-ray absorption spectra at the transition-metal L₃-edges are highly sensitive to the valence state. Compared to standard CoO(2+), the Co L₃-edge peak energy of the as-synthesized samples exhibits a negative shift (Fig. S13†). More accurate atomic coordi-
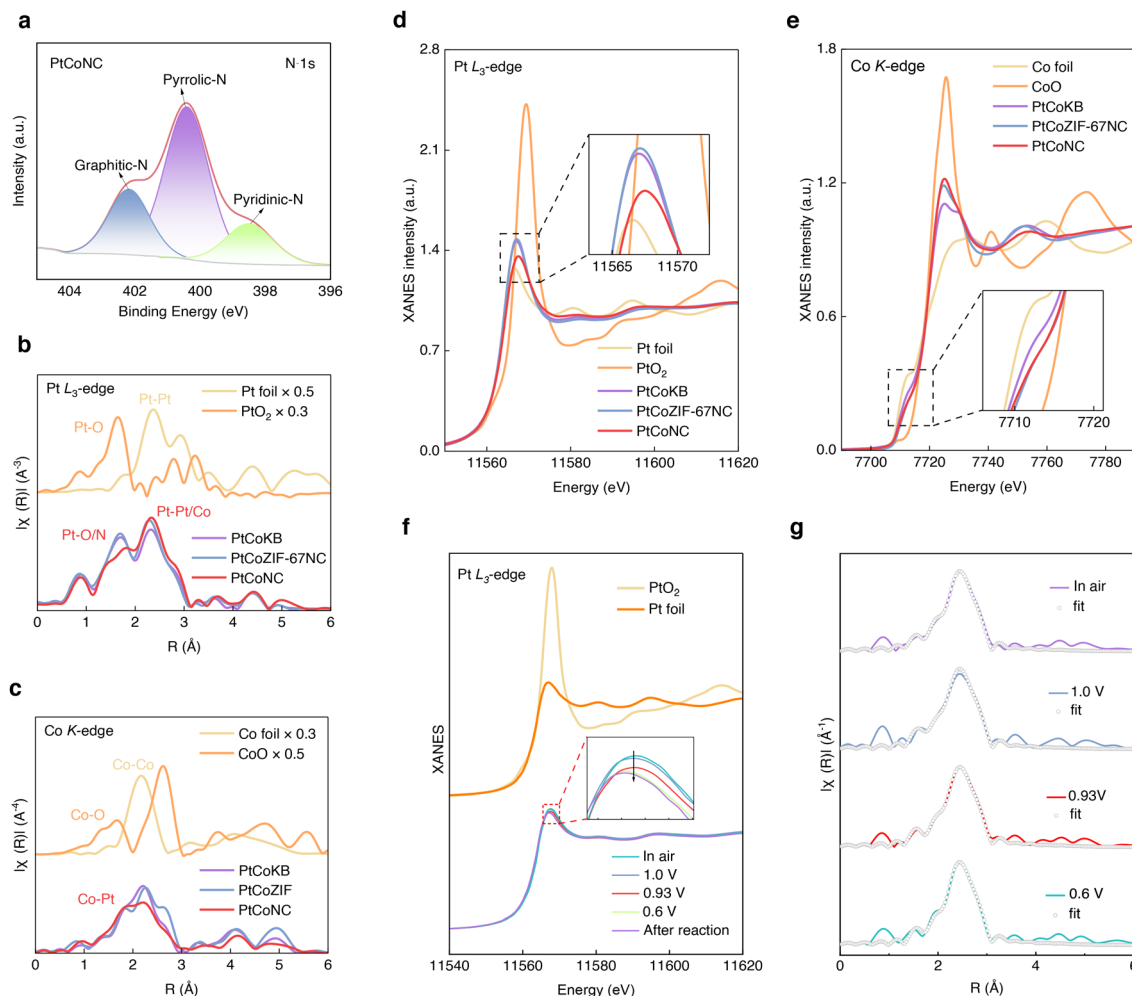
Fig. 3 (a) N 1s XPS spectrum. (b) Pt L_3-edge (c) Co K-edge of FT-EXAFS spectra for PtCoKB, PtCoZIF67 and PtCoNC. (d) Pt L_3-edge XANES spectra of Pt foil, PtCoNC, PtO_2, PtCoKB, PtCoZIF67 and PtCoNC. (e) Co K-edge XANES spectra of Co foil, CoO, PtCoZIF67 and PtCoNC. (f) *In situ* XANES spectra of Pt L_3-edge. Inset: Magnified white-line peak and pre-edge XANES region. (g) EXAFS curves of PtCoNC at In air, 1.0 V, 0.93 V and 0.6 V.

nation and local electronic structures of Co and Pt were characterized by X-ray absorption spectroscopy. X-ray absorption near-edge structure (XANES) results indicate that the valence state of Pt in PtCoNC is between Pt foil and PtO_2, and closer to Pt foil[26] (Fig. 3d), which is in good agreement with the XPS results. The absorption edge for Co is closer to Co foil, and a large shift to CoO was detected in PtCoNC, suggesting a similar electronic structure of Co foil (Fig. 3e). The evidently shorter Pt–Pt bond length of PtCoNC than that of Pt/C could be well ascribed to the smaller size of Co atoms compared with Pt, thus inducing the global stress. The Fourier transformed extended X-ray absorption fine structure (FT-EXAFS) spectra reveal a main scattering peak, assigning to the contribution of Pt–Pt/Pt–Co bonds. It is shorter than that of Pt foil, which could be well ascribed to the smaller size of Co atoms thus inducing the global stress (Fig. 3b). Additionally, the white-line peak of the Pt L_3-edge gives insight into the electron vacancy, showing a decreased integrated intensity. This result indicated an increasing 5d-electron density and charge

transfer from Co to Pt during the formation of intermetallic bonds.

To further probe the dynamic changes in the oxidation state and local coordination environment at the ORR-relevant potentials, *in situ* XAFS measurements were performed. Fig. 3g presents the evolutions of the normalized Pt L_3-edge XANES spectra. It shows the potential-dependent Pt-L_3 edge XANES of PtCoNC, emphasizing the metallic state of Pt at 0.6 V, 0.93 V and 1.0 V (*vs.* RHE). Comparatively, the normalized white-line intensity at the Pt L_3-edge decreased with decreasing the applied potentials, indicating a slight decrease in oxidation state. When the voltage was applied from 1.0 to 0.6 V (*vs.* RHE), the peak intensity of the white-line decreased because of the chemisorption of surface oxygenated species (*OH, *OOH and/or *O).[27] The EXAFS of the Pt L_3-edge of Pt foil shows a feature at 2.39 Å, corresponding to the Pt–Pt/Pt–Co coordination (Fig. S14†). The shift is due to the change of the Pt–Pt bond distance. Compared with Pt foil, the main peak shifted to the lower R position, which is a consequence of high

contraction strain. Such a phenomenon suggests an electron transition from adjacent atoms to Pt sites, which can potentially enhance the catalytic reaction rate. As shown in Fig. 3f, the spectra of PtCoNC at various potentials are all similar, indicating the structural retention during the cycling experiments. Furthermore, as the applied cell voltage decreases from 1.0 to 0.6 V (vs. RHE), the Pt–Co configuration remains stable (Fig. 3g and Table S2†).

In order to further study the electrocatalytic reaction mechanism on metal surfaces and detect various adsorbed oxygenated intermediate species, the *in-situ* synchrotron radiation Fourier transform infrared spectroscopy (SR-FTIR) technique was employed, by varying the potential (E) stepwise from 1.0 V vs. RHE down to 0.05 V vs. RHE in dioxygen-saturated 0.1 M $HClO_4$ solution. Initial observations in Fig. S18† indicate the absence of significant peaks near the starting potential. As shown in Fig. 4a, the peak at 1143 cm^{-1} corresponds to the

*OOH intermediate. As the potential decreases, the kinetics of the ORR is accelerated and the peak intensity of *OOH begins to appear.[28] A subsequent peak at 968 cm^{-1} is assigned to *O, which is the key intermediate of the four-electron reaction pathway. The broad peak ranging between 3600–3800 cm^{-1} is mainly due to the tensile vibration of *OH, signifying the formation of water, a key intermediate species (Fig. 4b). As the potential becomes negative, the peak intensity increases, indicating a heightened hydroxyl adsorption at the active sites. With increasing time, the peak of *OH remains stable (Fig. S19†). This stability can be attributed to the facilitated *OH desorption during the ORR process, highlighting the predominance of rapid four-electron reactions.[29]

On the basis of these experimental data, density functional theory (DFT) analysis was performed to understand the origin of the improved ORR catalytic activities. The PtCo nanoparticles are supported on the N-doped composite carbon
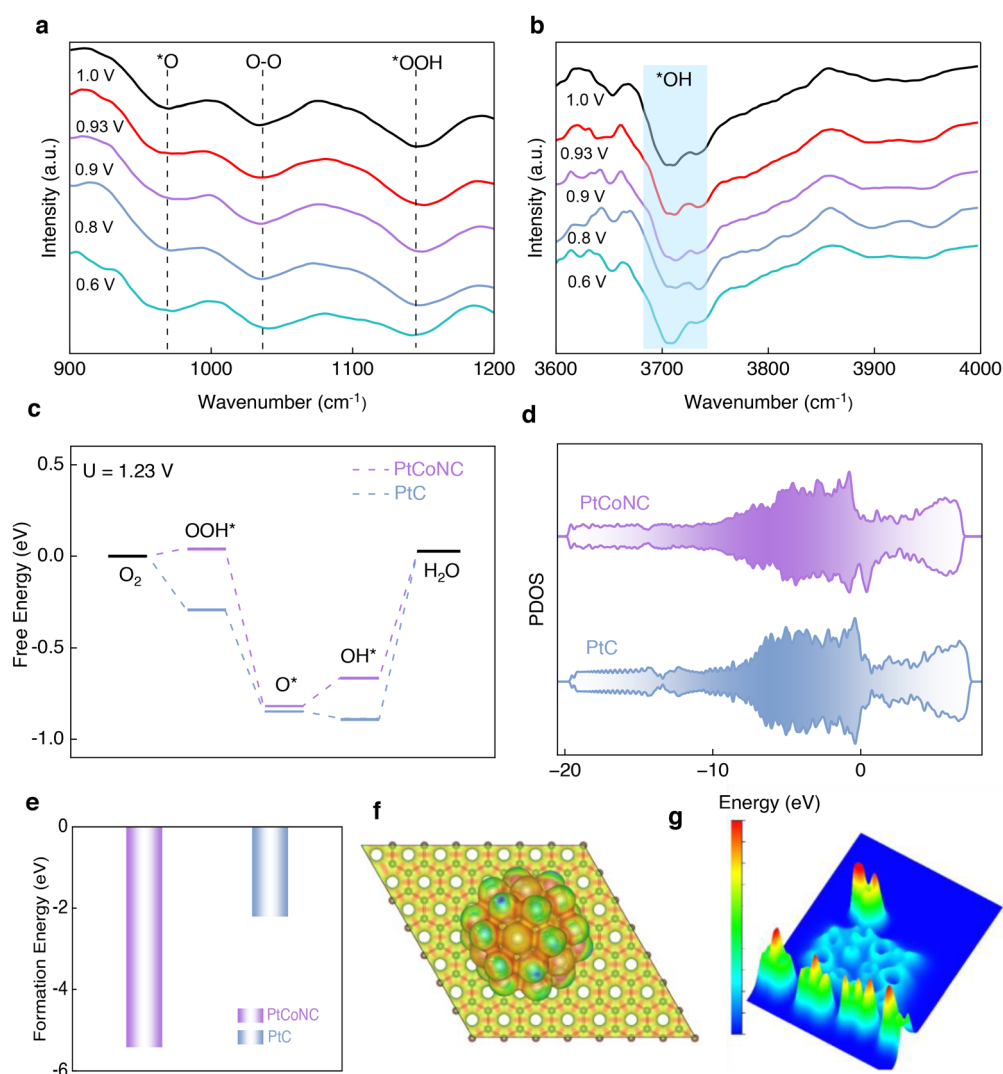

Fig. 4 (a and b) The *in-situ* SR-FTIR spectra for PtCoNC. (c) The free energy diagram for the ORR on PtCoNC. (d) PDOS. (e) Formation energy between nanoparticles and supports. (f) Electrostatic potential maps for Pt/C. (g) The 3D electron localization function for adsorption of *OH on PtCoNC (red region represents electronic accumulation).

support according to the XRD and XAFS characterization results. PtCo(111) is regarded as the ORR active crystal plane of the catalyst to calculate the free energies of each elemental reaction step at U=1.23 and U=0 V. As shown in Fig. 4c, at U=1.23 V, it could be clearly identified that the rate-limiting step (RLS) of PtCoNC and PtC is the desorption of *OH (*OH + H^+ + e^- → H_2O), while the Gibbs free energy changes (ΔG) of formation of H_2O (PtCoNC and PtC) are 0.69 eV and 0.91 eV, respectively. Obviously, compared with Pt/C, the d-band center of Pt for PtCoNC was down-shifted, thus diminishing the absorption energy of Pt and oxygen-containing intermediates and improving the intrinsic ORR activity. The calculated free-energy diagram shows the exothermic reactions and spontaneous thermodynamically. The ΔG of formation of *O has the highest value indicating the four electron reaction process tendency.[30] Furthermore, the enhanced conductivity of PtCoNC is confirmed than that of Pt/C by the higher projected density of states (PDOS) near the Fermi level (Fig. 4d). And the d-band center (ε_d) is calculated to be −2.61 and −2.59 eV, respectively. It is well illustrated that the higher binding energy unveils the stronger interaction between PtCo nanoparticles and supports (Fig. 4e). The results indicate that the enhanced intrinsic activity of PtCoNC could be attributed to the relatively weakened adsorption of intermediate species, and the lowest free energy for RLS (*OH desorption process) with appropriate modification of the electronic structure and geometric structure with designed supports. The 3D maps of the electron localization function (ELF) (Fig. 4f) clearly show the electron transfer from Co to Pt when adsorption of the *OH intermediate occurs, indicating a robust covalent modulation effect of Co and Pt. Thus, the above results demonstrate that the interaction between nanoparticles and composite supports is enhanced, hence weakening the migration and aggregation of PtCo nanoparticles and increasing the stability of PtCoNC. In a nutshell, DFT calculations explain that the improvement of ORR properties is mainly assigned to the optimized RLS, strengthened metal–carrier interaction and down-shifted d-band center. In a word, the alloy effect and enhanced metal–support interaction contribute to the enhanced ORR intrinsic activity of PtCoNC.

Conclusions

In summary, we have rationally conceived and successfully synthesized uniform ultrafine PtCo alloy particles on a distinctive composite support, exhibiting a remarkable enhancement in ORR activity compared to conventional supports. Importantly, ADT results revealed a mere 5% loss of the ECSA after the stability testing. The support has a porosity level required for good catalytic performance; micropores limit the active site, while the mesoporous structure amplifies accessibility and molecular transport. In combination of synchrotron radiation *in situ* XAFS, *in-situ* FTIR technology and DFT calculations, we clarify that the hybrid catalysts strengthen the synergistic ORR catalysis and stability. Furthermore, the catalysts exhibit out-

standing performance in hydrogen–oxygen fuel cells, achieving a high power density of 1.83 W cm^{-2} at 4 A cm^{-2}. This research introduces a streamlined and effective methodology for developing supported Pt-based alloy catalysts, paving the way for the fabrication of high-efficiency and enduring fuel cell catalysts.

Author contributions

Tao Yao, Lingling Zhang, Wei Zhang and Tao Ding conceptualized the work and wrote the manuscript. Lingling Zhang performed the sample preparation and characterization and ORR measurements. Xiaokang Liu performed the XAFS measurements. Tong Liu and Qiquan Luo performed the DFT calculations. Sicheng Li and Xue Zhang provided drawing suggestions. All authors have approved the final version of the manuscript.

Conflicts of interest

There are no conflicts to declare.

Acknowledgements

References

1 L. Huang, M. Wei, R. Qi, C. L. Dong, D. Dang, C. C. Yang, C. Xia, C. Chen, S. Zaman, F. M. Li, B. You and B. Y. Xia, An integrated platinum-nanocarbon electrocatalyst for efficient oxygen reduction, *Nat. Commun.*, 2022, **13**, 6703.

2 K. Kodama, T. Nagai, A. Kuwaki, R. Jinnouchi and Y. Morimoto, Challenges in applying highly active Pt-based nanostructured catalysts for oxygen reduction reactions to fuel cell vehicles, *Nat. Nanotechnol.*, 2021, **16**, 140–147.

3 F. Cao, H. Zhang, X. Duan, X. Li, R. Ding, K. Hua, Z. Rui, Y. Wu, M. Yuan, J. Wang, J. Li, M. Han and J. Liu, Coating Porous TiO_2 Films on Carbon Nanotubes to Enhance the Durability of Ultrafine PtCo/CNT Nanocatalysts for the

Oxygen Reduction Reaction, *ACS Appl. Mater. Interfaces*, 2022, **14**, 51975–51982.

4 J. Qin, P. Zou, R. Zhang, C. Wang, L. Yao and H. L. Xin, Pt–Fe–Cu Ordered Intermetallics Encapsulated with N-Doped Carbon as High-Performance Catalysts for Oxygen Reduction Reaction, *ACS Sustainable Chem. Eng.*, 2022, **10**, 14024–14033.

5 X. X. Wang, S. Hwang, Y.-T. Pan, K. Chen, Y. He, S. Karakalos, H. Zhang, J. S. Spendelow, D. Su and G. Wu, Ordered Pt₃Co Intermetallic Nanoparticles Derived from Metal–Organic Frameworks for Oxygen Reduction, *Nano Lett.*, 2018, **18**, 4163–4171.

6 M. Wei, L. Huang, L. Li, F. Ai, J. Su and J. Wang, Coordinatively Unsaturated PtCo Flowers Assembled with Ultrathin Nanosheets for Enhanced Oxygen Reduction, *ACS Catal.*, 2022, **12**, 6478–6485.

7 D. Bhalothia, L. Krishnia, S.-S. Yang, C. Yan, W.-H. Hsiung, K.-W. Wang and T.-Y. Chen, Recent Advancements and Future Prospects of Noble Metal-Based Heterogeneous Nanocatalysts for Oxygen Reduction and Hydrogen Evolution Reactions, *Appl. Sci.*, 2020, **10**, 7708.

8 Y.-J. Wang, N. Zhao, B. Fang, H. Li, X. T. Bi and H. Wang, A highly efficient PtCo/C electrocatalyst for the oxygen reduction reaction, *RSC Adv.*, 2016, **6**, 34484–34491.

9 Z. Zhao, Z. Liu, A. Zhang, X. Yan, W. Xue, B. Peng, H. L. Xin, X. Pan, X. Duan and Y. Huang, Graphene-nano-pocket-encaged PtCo nanocatalysts for highly durable fuel cell operation under demanding ultralow-Pt-loading conditions, *Nat. Nanotechnol.*, 2022, **17**, 968–975.

10 T. Soboleva, K. Malek, Z. Xie, T. Navessin and S. Holdcroft, PEMFC catalyst layers: the role of micropores and mesopores on water sorption and fuel cell activity, *ACS Appl. Mater. Interfaces*, 2011, **3**, 1827–1837.

11 H. Cheng, R. Gui, H. Yu, C. Wang, S. Liu, H. Liu, T. Zhou, N. Zhang, X. Zheng, W. Chu, Y. Lin, H. Wu, C. Wu and Y. Xie, Subsize Pt-based intermetallic compound enables long-term cyclic mass activity for fuel-cell oxygen reduction, *Proc. Natl. Acad. Sci. U. S. A.*, 2021, **118**, e2104026118.

12 T.-W. Song, C. Xu, Z.-T. Sheng, H.-K. Yan, L. Tong, J. Liu, W.-J. Zeng, L.-J. Zuo, P. Yin, M. Zuo, S.-Q. Chu, P. Chen and H.-W. Liang, Small molecule-assisted synthesis of carbon supported platinum intermetallic fuel cell catalysts, *Nat. Commun.*, 2022, **13**, 6521.

13 D. A. Cullen, K. C. Neyerlin, R. K. Ahluwalia, R. Mukundan, K. L. More, R. L. Borup, A. Z. Weber, D. J. Myers and A. Kusoglu, New roads and challenges for fuel cells in heavy-duty transportation, *Nat. Energy*, 2021, **6**, 462–474.

14 S. Li, W. Xie, Y. Song, Y. Li, Y. Song, J. Li and M. Shao, Integrated CoPt electrocatalyst combined with upgrading anodic reaction to boost hydrogen evolution reaction, *Chem. Eng. J.*, 2022, **437**, 135473.

15 P. Guo, Y. Xia, B. Liu, M. Ma, L. Shen, Y. Dai, Z. Zhang, Z. Zhao, Y. Zhang, L. Zhao and Z. Wang, Low-Loading Sub-3 nm PtCo Nanoparticles Supported on Co–N–C with Dual Effect for Oxygen Reduction Reaction in Proton Exchange Membrane Fuel Cells, *ACS Appl. Mater. Interfaces*, 2022, **14**, 53819–53827.

16 W. Yang, P. Cheng, Z. Li, Y. Lin, M. Li, J. Zi, H. Shi, G. Li, Z. Lian and H. Li, Tuning the Cobalt–Platinum Alloy Regulating Single-Atom Platinum for Highly Efficient Hydrogen Evolution Reaction, *Adv. Funct. Mater.*, 2022, **32**, 2205920.

17 T. E. O'Brien, S. Herrera, D. A. Langlois, N. N. Kariuki, H. Yu, M. J. Zachman, D. J. Myers, D. A. Cullen, R. L. Borup and R. Mukundan, Impact of Carbon Support Structure on the Durability of PtCo Electrocatalysts, *J. Electrochem. Soc.*, 2021, **168**, 054517.

18 X. Xie, L. Shang, X. Xiong, R. Shi and T. Zhang, Fe Single-Atom Catalysts on MOF-5 Derived Carbon for Efficient Oxygen Reduction Reaction in Proton Exchange Membrane Fuel Cells, *Adv. Energy Mater.*, 2021, **12**, 2102688.

19 S. Ott, A. Orfanidi, H. Schmies, B. Anke, H. N. Nong, J. Hübner, U. Gernert, M. Gliech, M. Lerch and P. Strasser, Ionomer distribution control in porous carbon-supported catalyst layers for high-power and low Pt-loaded proton exchange membrane fuel cells, *Nat. Mater.*, 2019, **19**, 77–85.

20 P. J. Pérez-Díaz, A. Medina-Ramírez, I. R. G. Esquivel, G. G. Ruiz and B. Ruiz-Camacho, Effect of X zeolite-carbon composite ratio as support of Pt nanoparticles for MOR and ORR, *Ionics*, 2021, **27**, 1813–1828.

21 Y. Li, Y. Li, E. Zhu, T. McLouth, C. Y. Chiu, X. Huang and Y. Huang, Stabilization of high-performance oxygen reduction reaction Pt electrocatalyst supported on reduced graphene oxide/carbon black composite, *J. Am. Chem. Soc.*, 2012, **134**, 12326–12329.

22 Y. Gao, J. Zhao, J. Lian, X. Chen, Q. Zhu and X. Wang, Co–N as a Promoter towards Modulation Surface Chemistry of PtCo Alloy on 2D Thin Layer Hierarchical Porous Nitrogen–Carbon for the Efficient Oxygen Reduction Reaction, *ChemistrySelect*, 2022, **7**, e20220121.

23 S. Di, C. Guo, Y. Dai, F. Wang, Z. Wang and H. Zhu, Nitrogen-Doped Porous Carbon-Supported PtCo Nanoparticle Electrocatalyst for Oxygen Reduction Reaction Prepared by a Dual-Template Method, *ACS Appl. Energy Mater.*, 2023, **6**, 1639–1649.

24 V. Yarlagadda, M. K. Carpenter, T. E. Moylan, R. S. Kukreja, R. Koestner, W. Gu, L. Thompson and A. Kongkanand, Boosting Fuel Cell Performance with Accessible Carbon Mesopores, *ACS Energy Lett.*, 2018, **3**, 618–621.

25 M. Chen, S. Zhou, W. Liao, Z. Wang, J. Long, Q. Zhou and Q. Wang, Ordered PtCo Intermetallics Featuring Nitrogen-Doped Carbon Prepared by Surface Coating Strategy for Oxygen Reduction Reaction, *ChemElectroChem*, 2022, **9**, e202200803.

26 B. Pang, C. Jia, S. Wang, T. Liu, T. Ding, X. Liu, D. Liu, L. Cao, M. Zhu, C. Liang, Y. Wu, Z. Liao, J. Jiang and T. Yao, Self-Optimized Ligand Effect of Single-Atom Modifier in Ternary Pt-Based Alloy for Efficient Hydrogen Oxidation, *Nano Lett.*, 2023, **23**, 3826–3834.

27 W. Zhou, H. Su, W. Cheng, Y. Li, J. Jiang, M. Liu, F. Yu, W. Wang, S. Wei and Q. Liu, Regulating the scaling

relationship for high catalytic kinetics and selectivity of the oxygen reduction reaction, *Nat. Commun.*, 2022, **13**, 6414.

28 S. Kukunuri and H. Noguchi, In Situ Spectroscopy Study of Oxygen Reduction Reaction Intermediates at the Pt/Acid Interface: Surface-Enhanced Infrared Absorbance Spectroscopy, *J. Phys. Chem. C*, 2020, **124**, 7267–7273.

29 S. Nayak, I. J. McPherson and K. A. Vincent, Adsorbed Intermediates in Oxygen Reduction on Platinum Nanoparticles Observed by In Situ IR Spectroscopy, *Angew. Chem., Int. Ed.*, 2018, **57**, 12855–12858.

30 X. Cheng, Y. Wang, Y. Lu, L. Zheng, S. Sun, H. Li, G. Chen and J. Zhang, Single-atom alloy with Pt-Co dual sites as an efficient electrocatalyst for oxygen reduction reaction, *Appl. Catal., B*, 2022, **306**, 121112.

31 L. C. Sun, Y. Z. Qin and Y. Yin, ZIF derived PtCo alloys-based nitrogen-doped graphene as cathode catalyst for proton exchange membrane fuel cell, *J. Power Sources*, 2023, **562**, 232758.

32 L. Chong, *et al.*, Ultralow-loading platinum-cobalt fuel cell catalysts derived from imidazolate frameworks, *Science*, 2018, **362**, 1276–1281.